

# Soft and elastic hydrogel-based microelectronics for localized low-voltage neuromodulation

Yuxin Liu<sup>1,4</sup>, Jia Liu<sup>2,4</sup>, Shucheng Chen<sup>2</sup>, Ting Lei<sup>2</sup>, Yeongin Kim<sup>3</sup>, Simiao Niu<sup>2</sup>, Huiliang Wang<sup>1</sup>, Xiao Wang<sup>1</sup>, Amir M. Foudeh<sup>2</sup>, Jeffrey B.-H. Tok<sup>2</sup> and Zhenan Bao<sup>1,2\*</sup>

**Narrowing the mechanical mismatch between tissue and implantable microelectronics is essential for reducing immune responses and for accommodating body movement. However, the design of implantable soft electronics (on the order of 10 kPa in modulus) remains a challenge because of the limited availability of suitable electronic materials. Here, we report electrically conductive hydrogel-based elastic microelectronics with Young's modulus values in the kilopascal range. The system consists of a highly conductive soft hydrogel as a conductor and an elastic fluorinated photoresist as the passivation insulation layer. Owing to the high volumetric capacitance and the passivation layer of the hydrogel, electrode arrays of the thin-film hydrogel 'elastronics', 20  $\mu\text{m}$  in feature size, show a significantly reduced interfacial impedance with tissue, a current-injection density that is  $\sim 30$  times higher than that of platinum electrodes, and stable electrical performance under strain. We demonstrate the use of the soft elastronic arrays for localized low-voltage electrical stimulation of the sciatic nerve in live mice.**

Implantable neuromodulation devices, such as deep brain stimulators and vagus nerve stimulators, have been widely used to treat neurological diseases<sup>1,2</sup>. However, such devices are made of rigid probes and are limited by both the low spatial resolution and mechanical mismatch with tissues<sup>3</sup>. Utilizing soft microelectronic devices that possess similar mechanical properties as biological systems will provide both stable and intimate electrical coupling with electrogenic neural tissues for localized and efficient electrical stimulation. In addition, recent studies have suggested that reduced mechanical mismatch across the electronics–tissue interface elicits significantly fewer adverse immune responses for chronic implantation<sup>4,5</sup>. Indeed, designing soft and compliant electronics has been actively pursued for neuroprosthetics and human–machine interfaces<sup>6–12</sup>. Most approaches have focused on the structural design of the electronics, such as ultrathin electronics and macroporous mesh structures<sup>11,13</sup> to decrease the bending stiffness or stretchable electronics enabled by strain engineering using rigid components<sup>10,14</sup>. An alternative approach to make stretchable microelectronics with low bending stiffness is to develop intrinsically stretchable electronic materials with a low Young's modulus, which offers tissue-level soft mechanical properties without constraints on the geometry of the electronics and the direction of applied strain.

Owing to its tissue-mimicking mechanical properties, hydrogels have been widely used in cell cultures<sup>15</sup>, soft tissue adhesives<sup>16,17</sup> and implantations<sup>18</sup>. The excellent ionic conduction of elastic hydrogel electronics also allows them to be used as electrodes for artificial muscle<sup>19</sup>. Unfortunately, a pure ionic hydrogel lacks electronic conductivity and the slow ion movement results in a slow response time, preventing them from interrogating high-speed ( $>1,000$  Hz) single-neuron-single-spike neural activity. A conductive polymer (CP) printed on a hydrogel<sup>20,21</sup> and a conductive hydrogel coating on rigid electrodes<sup>22–24</sup> have been previously reported to narrow the mechanical gap at the bioelectronic interface. Efforts have also been made to prepare electrically conductive hydrogels (ECHs) by mixing a CP or an in situ polymerized CP in a hydrogel matrix<sup>25–31</sup>. However, low electrical conductivity and lack of convenient

methods for micropatterning prevents the miniaturization of soft electronics and therefore their applications for precise neuromodulation in vivo. In addition, hermetic encapsulation systems, which are required to prevent leakage current and to achieve localized neuromodulation, in general are made of materials with a high Young's modulus (greater than gigapascal)<sup>32,33</sup>. There is also a lack of choice regarding suitable materials for micropatterning and with soft elastomer and low permeability properties. Stretchable insulating materials that are compatible with microfabrication and have a Young's modulus similar to that of soft tissues need to be developed. In this work, we report a thin-film elastronic that can interface with peripheral nerves for localized neuromodulation (Fig. 1a). The organization of the paper is as follows. First, we introduce a method to prepare a highly conductive ECH to ensure the required conductance when patterned into a microscale thin-film structure. Next, we present a stretchable insulation material whereby its Young's modulus is tuned to match that of nerve tissue. Subsequently, we describe the lithographical process developed to pattern the two soft and intrinsically stretchable materials into a multielectrode array. Furthermore, we report data validating its aqueous stability and biocompatibility for chronic implantation. Finally, we demonstrate it can produce effective electrical stimulation with high current density at ultralow voltages in a mouse model in vivo.

## A highly electrically conductive hydrogel

The low conductivity of ECHs has previously limited their application as electrodes and interconnects, especially when microscale patterning is needed. Previously, we reported that blending certain ionic liquids into the CP solution poly(3,4-ethylenedioxythiophene):poly(styrenesulfonate) (PEDOT:PSS) could promote the aggregation of PEDOT polymers. This resulted in an ion gel film with an interconnected CP network<sup>34</sup>. Here, we removed the ionic liquid additive via water exchange (Supplementary Figs. 1 and 2), which subsequently transformed the ion gel into a hydrogel (Fig. 1b). We observed that the electronic conductance of the ECH remained stable after removal of the ionic liquid and was significantly higher

<sup>1</sup>Department of Bioengineering, Stanford University, Stanford, CA, USA. <sup>2</sup>Department of Chemical Engineering, Stanford University, Stanford, CA, USA.

<sup>3</sup>Department of Electrical Engineering, Stanford University, Stanford, CA, USA. <sup>4</sup>These authors contributed equally: Yuxin Liu, Jia Liu. \*e-mail: [zbao@stanford.edu](mailto:zbao@stanford.edu)

than the corresponding ionic conductance (Supplementary Fig. 3). Our ECH has an electrical conductivity of  $47.4 \pm 1.2 \text{ S cm}^{-1}$  (Fig. 1c), and this value represents one of the highest reported for an ECH<sup>35</sup>. The water content in the hydrogel was estimated to be  $\sim 82 \text{ wt}\%$  within 1 min of soaking in water, and stabilized at  $85 \text{ wt}\%$  (Fig. 1d).

Next, to understand the origin of the high electrical conductivity of the ECH, we characterized both the compositional and morphological changes during the ion gel to hydrogel transition. First, X-ray photoelectron spectroscopy (XPS) measurements showed that the ratio between PEDOT and PSS increased from 0.4 to 0.78 after washing with water (Fig. 1e; Supplementary Fig. 4). This suggests that excessive PSS may have been partially washed away, thus further improving the continuity of the interconnected PEDOT network and reducing the ratio of the electronically insulating PSS, which may impede electronic conduction<sup>36,37</sup>. Second, scanning electron microscopy (SEM) images showed that after removal of the ionic liquid, the dried ECH collapsed into  $\sim 1 \mu\text{m} \times 200 \text{ nm}$  ellipse-shaped voids with slight in-plane alignment (Fig. 1b(ii)). When rehydrated (Fig. 1b(iii)), we observed a rapid anisotropic volume expansion in the out-of-plane direction (Supplementary Video 1), while maintaining the in-plane connectivity between PEDOT domains. By contrast, without the ionic liquid modification, the PEDOT:PSS film exhibited a thick-layered structure containing larger gaps ( $>30 \mu\text{m}$ ) between layers (Supplementary Fig. 5), thus preventing effective interconnected structures. Taken together, the removal of the electronically insulating PSS improved PEDOT polymer network connectivity and reduced the ratio of the electronically insulating polymer, which collectively contributed to the high conductivity of the ECH.

### Soft conductive hydrogel and fluorinated elastomer

Electrodes that have strain-insensitive interfacial impedance are important for stable neuromodulation *in vivo*. Our ECH electrode (200 nm in thickness) sustained up to 20% strain (Fig. 1f) and compression (Supplementary Fig. 6). Specifically, under 10% strain, we observed that there was a  $<20\%$  and 3.6% impedance increase for an ECH film measured at 1 kHz and 1 Hz, respectively (Supplementary Fig. 7). The phase plot of the impedance spectrum showed that the ECH electrode reached a stable phase angle after stretch, with a phase angle close to  $0^\circ$  in the frequency range of 0.1–10 kHz. In addition, impedance showed a relatively stable impedance from 1 Hz to 1 MHz under a 20% uniaxial strain (Fig. 1g) and 15-kPa compressive pressure (Supplementary Fig. 8). We also performed a repeated stretch-and-release experiment on the ECH electrode for 10,000 cycles. We observed stable resistance and increased conductivity within the initial stretching and unloading cycle, potentially as a result of the chain alignment phenomenon<sup>34</sup>. For the resistance change over cycles, we observed a gradual increase from 1 to 1,000 cycles, which may be caused by structural damage to the ECH under the repeated stretching–loading process. Resistance then became stabilized at a more constant value from 1,000 to 10,000 cycles (Supplementary Fig. 9).

Tissue-level Young's modulus values for both stretchable conductors and insulation polymers are needed to reduce the mechanical mismatch between soft tissue and elastronics. The Young's modulus values of the ECH were estimated to be  $32 \pm 5.1 \text{ kPa}$  when measured via compression tests (Fig. 1h) and  $24 \pm 5.4 \text{ kPa}$  when measured via nanoindentation experiments using an atomic force microscope (AFM) (Supplementary Fig. 10). In addition, we carefully tuned the Young's modulus of the UV-crosslinked dimethacrylate-functionalized perfluoropolyether (PFPE-DMA) monomer (Fig. 1i) to be  $<30 \text{ kPa}$  (Fig. 1j) by using a PFPE-DMA with a number averaged molecular weight of 12 kDa. The resulting UV-crosslinked elastomer was stretchable up to 200% without incurring any fracture and with a low dielectric constant of  $2.4 \pm 0.1$  (Supplementary Fig. 11). The Young's modulus of our ECH was four to six orders of magnitude

lower than that of commonly used conductors such as platinum and PEDOT:PSS, while the Young's modulus of PFPE-DMA was two to six orders of magnitude lower than dielectric materials such as polydimethylsiloxane (PDMS) and polyimide. In addition, the modulus values of both materials were comparable to soft tissue, for example, nerve tissue<sup>38,39</sup> (Fig. 1k).

### Lithographically micropatterned ECH electrodes

Patterning continuous hydrogel electrodes over a centimetre-scale area at sub-100- $\mu\text{m}$  resolution remains a challenging feat. Current methods employ inkjet printing to pattern hydrogels<sup>40</sup>. However, the resultant patterned structures suffer from rough surfaces and discontinuity, hence limiting the feature size to mostly  $>100 \mu\text{m}$ . Meanwhile, traditional micropatterning by lithography and etching are not possible for direct patterning of hydrogels because of their highly porous structure and high water content. However, our ion gel allows a unique opportunity for using traditional photolithographic patterning, which is subsequently converted into a micropatterned ECH (MECH) by water exchange. As such, we can easily pattern any desired geometries with a resolution down to  $5 \mu\text{m}$  (Fig. 2a; Supplementary Figs. 12 and 13).

Next, we developed a general strategy to directly pattern a stretchable insulation layer with microscale resolution. Most elastomers are easily swelled by either our ionic liquid-modified PEDOT:PSS or various organic solvents commonly used in photolithography. In addition, micropatterning of the stretchable insulation layer directly above the polymeric conductor has not been reported before. To address both challenges, we developed a fluorinated elastic photoresist using PFPE-DMA. Using conventional photolithography tools, we could directly photopattern PFPE-DMA with arbitrary and complex geometries with feature sizes down to  $1.5 \mu\text{m}$  (Fig. 2b; Supplementary Fig. 14). Following UV exposure, this stretchable photoresist became highly elastic, stretchable and chemically stable in most common solvents.

By using the micropatterning strategy described above, we fabricated a thin-film elastronic electrode array (Fig. 2c,d) by combining the MECH as the stretchable electrode and PFPE-DMA as both the top and bottom elastomeric encapsulation layers (Supplementary Fig. 15). MECH electrodes ( $20\text{-}\mu\text{m}$  wide) were patterned photolithographically, with Au as the hard mask for etching. It is worth noting that the anisotropic swelling property of the MECH was maintained in the in-plane dimension of the electrode without distortion, with a swelling ratio of 2.1 when sandwiched by the elastic PFPE-DMA (Supplementary Fig. 16). PFPE-DMA, as a photoresist, was directly photopatterned onto the MECH as a top insulation layer (Fig. 2e). The freestanding device was stretchable by 20% without incurring cracks (Fig. 2f).

### Aqueous stability and biocompatibility

Although ECHs in general offer excellent mechanical properties for neural interfaces<sup>28,41,42</sup>, the lack of facile micropatterning techniques, together with the slow dissolution of CPs in ECHs, especially in a thin-film device structure, prevent the realization of microscale ECH devices for electrophysiological applications<sup>43–47</sup>. By comparison, our ECH exhibited a tissue-level Young's modulus and excellent stability in aqueous media (Supplementary Fig. 17). We quantified the stability of an ECH thin film ( $1.4 \mu\text{m}$ ) in water using UV–visible spectroscopy by monitoring the absorbance change at 800 nm, that is, the  $\pi\text{-}\pi$  transition in the PEDOT polymer. Notably, after 48 h of soaking in water, the ECH film showed only a slight decrease in UV–visible absorption intensity. By contrast, the absorption at 800 nm completely disappeared for a regular PEDOT:PSS thin film (Supplementary Fig. 18) after only 6 h of soaking in water. We attribute the significantly improved aqueous stability of our ECH film to a high density of physical crosslinks due to  $\pi\text{-}\pi$  interactions between PEDOT chains (Supplementary Fig. 19).

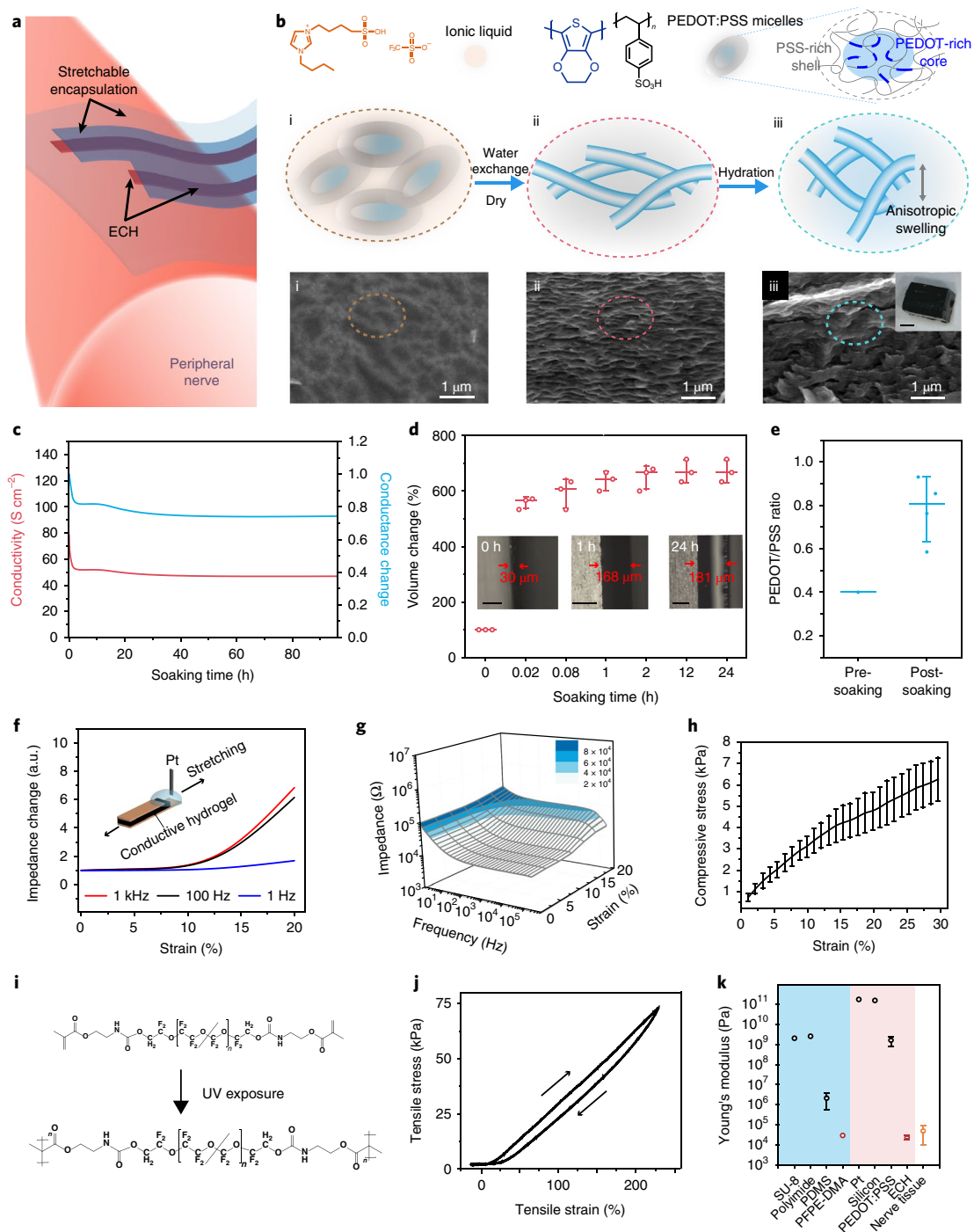


**Fig. 1 | An ECH and stretchable encapsulation material with tissue-level Young's modulus.** **a**, Schematic of the bioelectronic interface between a peripheral nerve and soft conductor electrodes and insulation materials. **b**, Schematic of the stepwise PEDOT:PSS ECH synthesis process and SEM images showing morphological changes in each step during the synthesis of an ECH. An ionic liquid, 4-(3-butyl-1-imidazolio)-1-butananesulfonic acid triflate, was blended with the PEDOT:PSS solution and subsequently dried to form an ion gel (i); ionic liquid is exchanged with water and then dried at room temperature (ii); the dried sample exhibits aligned and interconnected microstructures that swell in water to form the ECH (iii). The interconnected PEDOT polymer network in the ECH results in a continuous electronic conductive pathway. Scale bar, 1  $\mu m$  for the inset of (iii), which is an optical image of a hydrated ECH. **c**, d.c. conductance and conductivity change during the transition from ion gel to ECH by soaking in water over time. **d**, Volume change during the transition from ion gel to ECH ( $n=3$ ). Inset: side view of the sample changing from ion gel to ECH over time during soaking in water. Scale bar, 100  $\mu m$ . **e**, PEDOT/PSS ratio characterized by high-resolution XPS before and after washing ( $n=3$ ). **f**, Change in electrochemical impedance under different uniaxial strains at 1 Hz, 100 Hz and 1 kHz electrical field frequency. ECH film thickness is 200 nm at 0% strain. a.u., arbitrary units. Inset: schematic of the measurement set-up. ECH is sandwiched between elastomeric insulation layers. Physiological medium (DMEM) and a platinum electrode were employed as the electrolyte and the counter electrode, respectively. **g**, Surface plot of impedance at different strains and frequencies. **h**, Uniaxial stress-strain curve of the bulk ECH samples ( $n=3$ ). **i**, Molecular structure of elastic PFPE-DMA undergoing the crosslinking process following exposure to UV light. **j**, Uniaxial stress-strain curve of the crosslinked fluorinated elastic PFPE-DMA. **k**, Comparison of Young's modulus values between commonly used dielectric materials and the conductor with PFPE-DMA and ECH. Conductive and insulation materials are shaded in pink and blue, respectively. All error bars denote the s.d.

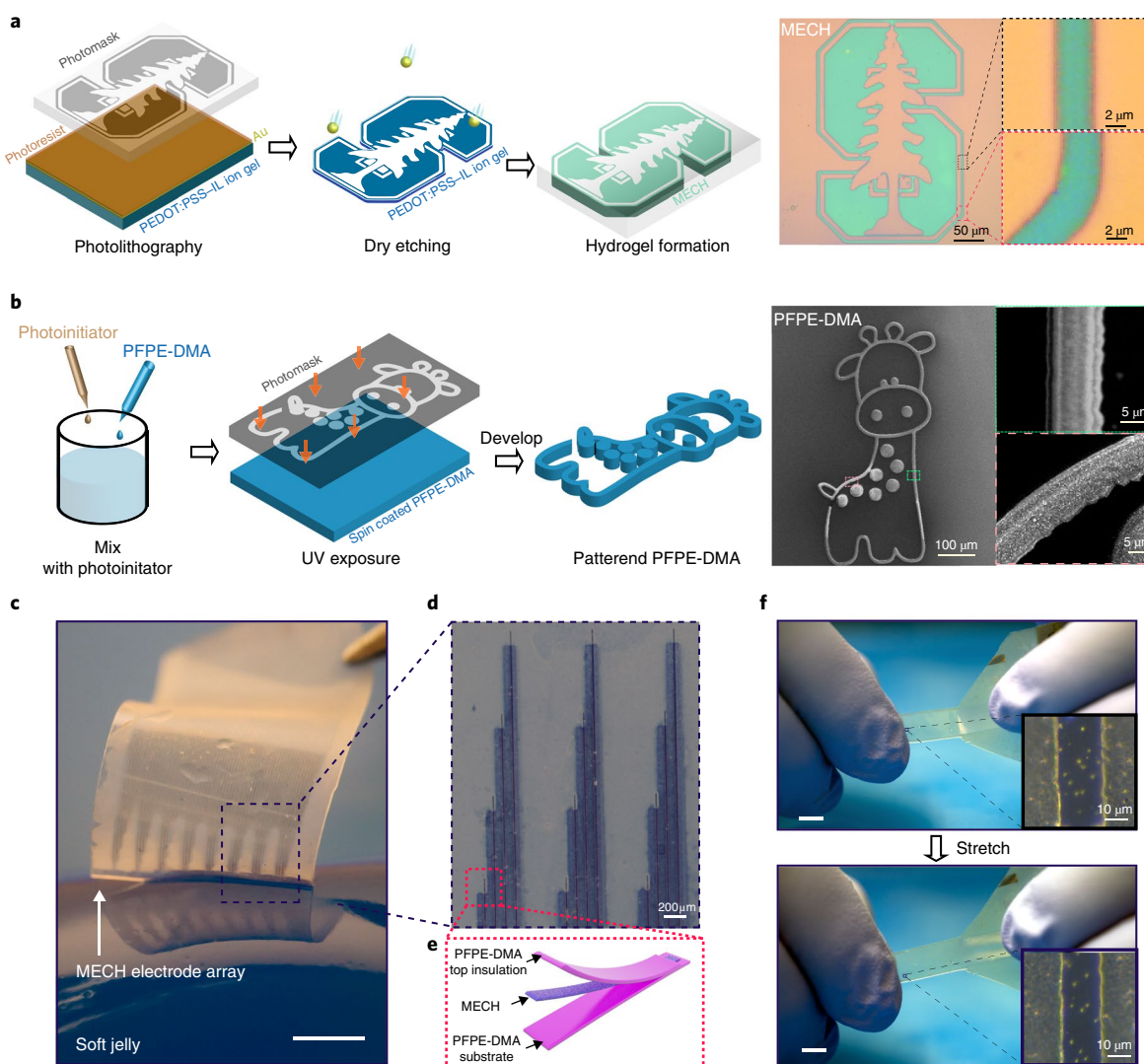


**Fig. 2 | Lithographically patterned hydrogel electronics.** **a**, Left: stepwise illustration of lithography of the MECH. Conventional photolithography was performed on PEDOT:PSS-ionic liquid (IL) ion gel with an Au hard mask. After that, the micropattern was transferred to the ion gel by dry etching. Finally, the micropatterned ion gel was transformed by water exchanging. Right: complex microstructures of the MECH, in which both straight and curved lines are resolved. **b**, Left: stepwise illustration for lithographically micropatterning of PFPE. PFPE-DMA was mixed with a photoinitiator and spun coated. UV light was used to crosslink the PFPE-DMA to form the micropattern. Right: SEM images of photolithographically micropatterned PFPE-DMA structures with both straight and curved lines. **c**, A freestanding MECH electronics electrode array pressed against soft jelly. Scale bar, 2 mm. **d**, Zoomed-in image of MECH electrodes (dark lines) with PFPE-DMA encapsulation (coloured as light blue). **e**, Schematic of an electronic electrode, a MECH electrode and interconnect sandwiched by photolithographically micropatterned fluorinated polymer PFPE-DMA as the top and bottom insulation layers. **f**, MECH electrode array stretched under 20% tensile strain shows no cracks. Scale bar, 5 mm. Inset: zoomed-in image of a MECH encapsulated in PFPE.

High charge storage capacity (CSC) and long-term stability in physiological conditions are both critical parameters to enable long-term neuromodulation<sup>48</sup>. Thus, we further investigated the electrochemical stability of the ECH thin-film devices by soaking it in PBS for 19 days. The current, as observed via cyclic voltammetry (CV), maintained a constant value over the entire incubation period (Supplementary Fig. 20). In addition, the ECH showed a CSC of  $164 \text{ mC cm}^{-2}$ , a value that is higher than that of electrochemically deposited PEDOT ( $75.6 \text{ mC cm}^{-2}$ )<sup>49</sup>, platinum ( $0.55 \text{ mC cm}^{-2}$ )<sup>50</sup>, IrOx ( $28.8 \text{ mC cm}^{-2}$ )<sup>49</sup>, a PEDOT-taurine conductive hydrogel ( $132 \text{ mC cm}^{-2}$ )<sup>51</sup> and a PEDOT-poly(vinyl alcohol)-heparin conductive hydrogel ( $80 \text{ mC cm}^{-2}$ )<sup>52</sup>. Moreover, the ECH maintained its high CSC value after 19 days of incubation, with less than 4.3% change (Fig. 3a). Furthermore, the MECH microelectrodes showed stable impedance when soaked in PBS for 19 days (Fig. 3b;

Supplementary Fig. 21). We characterized the capacity for insulation under different applied strains as well as under an AC bias for physiologically relevant voltages and frequencies. We observed that there were no significant changes in impedance for our fabricated freestanding MECH electronics at 20% strain (Fig. 3c), which can be explained by the excellent encapsulation capability of the low- $\kappa$  dielectric PFPE-DMA.

To evaluate the biocompatibility of our MECH electronics, we implanted the freestanding thin-film device ( $100 \mu\text{m}$  in thickness) by wrapping it around the sciatic nerve of mice and leaving it inside the freely moving mice for 6 weeks (Fig. 3d). Flexible plastic cuff electrodes (modulus of  $3.5 \text{ GPa}$ ,  $100 \mu\text{m}$  in thickness) made of polyethylene terephthalate (PET) and a thin film of Au were also implanted for comparison. Previous studies have suggested that the significant alteration of the biomechanical environment caused by

stiff cuff electrodes leads to fibrous tissue growth<sup>53,54</sup> and a reduced density of myelinated fibres<sup>55</sup>. We anticipated that the Young's modulus of the MECH electrode, which is in the range of nerve tissue and more than six orders of magnitude lower than conventional implantable probes<sup>56–58</sup> (Fig. 3e), would lead to a significantly reduced mechanical mismatch at the device–tissue interface and hence a reduced immune response. Confocal microscopy images of immunostained tissue slices (Supplementary Fig. 22) showed that compared with the sham control, there were no significant changes in the fluorescence intensities of neurofilaments and S-100 markers for Schwann cells at regions of the sciatic nerve with MECH electrode implantation. However, for the flexible plastic cuff electrode implant, while the fluorescence intensity of S-100 showed no significant change, the fluorescence intensity of neurofilaments was significantly reduced (Fig. 3f,g; Supplementary Fig. 23). We also characterized the level of the immune response by measuring the levels of the inflammatory biomarkers tumour necrosis factor- $\alpha$  (TNF- $\alpha$ ) and ED1. We observed that the plastic cuff electrodes induced significant growth of inflammatory tissue around the nerve bundles, which were labelled by anti-TNF $\alpha$  and anti-ED1 antibodies (Fig. 3h; Supplementary Fig. 24), while the MECH electrodes induced minimal inflammatory tissue growth. The inflammatory tissue areas for MECH electrode implants were comparable to that of the sham control and were significantly lower than that of the cuff electrodes (Fig. 3i). These results demonstrate that our implanted MECH electronics substantially reduced damage and inflammatory responses at peripheral neural tissues even under recurrent motion. This result suggests an enhanced biocompatibility of the MECH with tissue with dynamic motion. Previously, researchers<sup>59,60</sup> have demonstrated that immune responses can be substantially reduced by using ultrathin microelectronics at thickness of  $\sim 1 \mu\text{m}$ . While the decreased thickness contributes to reduced effective bending stiffness and a lower probe–tissue interfacial force, it may also bring difficulty for clinical applications that require vigorous handling of the implantable electronics. Our strategy of decreasing the Young's modulus provides an alternative way to reduce the effective bending stiffness without sacrificing ease of handling and surgical practicability. Together, the highly stable electrochemical performance in aqueous environment and the low immune response suggest that the MECH has promising clinical potential for long-term neuromodulation.

### Ultralow voltage neural stimulation

The porous microstructure of the MECH has the potential to enable excellent electrical and ionic dual conductivity<sup>61</sup> and high volumetric capacitance<sup>62,63</sup> in physiological solutions. Instead of using an ECH on the surfaces of metal electrodes as contact electrodes, as reported previously<sup>24,64</sup>, we employed the MECH as both the contact electrode and interconnect. We observed that the interconnect regions were also able to contribute to a further reduction in the overall impedance, since it is also partially filled with electrolyte. The obtained impedance was more than 10 times lower compared to an exposed Au electrode region coated with an ECH, and more than 20 times lower than coating with silane-crosslinked PEDOT:PSS with the same exposed electrode area (Fig. 4a). The phase plot of the impedance spectrum showed that the phase angle of the MECH is closer to  $0^\circ$  compared with the other two types of electrodes tested in the frequency range of 1–1,000 Hz, suggesting a resistance dominated impedance. To further investigate the contribution of the fabricated MECH interconnect to reducing the impedance, we next exposed only a cross-sectional area of the MECH for solution contact. Because the MECH interconnect was fabricated by swelling in Dulbecco's modified Eagle's media (DMEM), we compared the impedance resulting from a pure ionic conductor (DMEM) and from the dual conductive MECH electrode. Normalized to the same exposed electrode area, our MECH electrode showed three

orders of magnitude lower impedance compared to DMEM, and more than one order of magnitude lower impedance compared to platinum electrodes (Fig. 4b). We also calculated a capacitance of  $9,800 \mu\text{F cm}^{-2}$  (Supplementary Fig. 25) for our MECH electrode, which is higher than that of reported PEDOT:PSS ( $2,200 \mu\text{F cm}^{-2}$ )<sup>65</sup>. In addition, the MECH electrode showed a current density of  $1,359 \text{ mA cm}^{-2}$  under a bipolar pulsed voltage of 0.5 V at 50 Hz (Fig. 4c). This observed value is two to three orders of magnitude higher than that for electrodes made by DMEM ( $1 \text{ mA cm}^{-2}$ ) and platinum ( $48 \text{ mA cm}^{-2}$ ). It is also one order of magnitude higher than PEDOT:PSS ( $60 \text{ mA cm}^{-2}$ ; Supplementary Fig. 26) and one order of magnitude higher than the reported value for polyaniline ( $80 \text{ mA cm}^{-2}$ )<sup>66</sup>. The current density was relatively stable under compression or stretch, with a 7.5% decrease in amplitude for 15 kPa compressive pressure and a 33.5% decrease in amplitude for 20% uniaxial strain (Supplementary Fig. 27).

In either a pure electronic or ionic conductor, increasing the interconnect length with a fixed cross-sectional area will lead to a corresponding increase in the interconnect resistance and, thus, the overall impedance. However, the dual-conductive nature of the MECH resulted in increases in both the number of resistors ( $N_{R,\text{polymer}}$ ) in the equivalent circuits (which led to an increased electronic resistance) and the parallel interconnecting Randel circuits ( $n$ ) as the MECH length increased (Supplementary Fig. 28). This means that the effective solution contact area is significantly increased to much greater than just the exposed region of the micro-electrode due to the filling of solution into the MECH (Fig. 4d). As a result, our MECH design is particularly advantageous compared to previously reported CP electrodes in further reducing the interfacial impedance.

Next, based on the high electronic conductivity of our MECH, we hypothesized that the impedance reduction, which is due to the increased interfacial area from the encapsulated MECH interconnect, should surpass the negative effect from an increase in resistors ( $N_{R,\text{polymer}}$ ). To investigate the relationship between MECH interconnect length and interfacial impedance, we first measured both the impedance and the current density by varying only the length of the encapsulated MECH interconnects while maintaining the same width and thickness. We observed that as the interconnect length increased by 4.5 times, the impedance decreased by  $\sim 3.4$  times and the current density increased by 2.9 times, all in agreement with our hypothesis. Moreover, our simulation results showed a similar trend to that of the experimental data, in which the impedance decreased as the interconnect distance increased (Fig. 4e, inset; Supplementary Fig. 28). This suggests that the interconnect geometry can potentially be optimized to further reduce the impedance and increase current density. This understanding brought forth a new electrode design consideration unique to the MECH; that is, interconnect geometry. This is in addition to both the intrinsic electrode material properties and the electrode surface area of the MECH.

By optimizing our electrode design, we were able to deliver an excitation current density as high as  $10 \text{ mA cm}^{-2}$  at a low voltage of 50 mV (Supplementary Fig. 29) for neuromodulation. The MECH electrodes were placed in direct contact with the exposed sciatic nerve of anaesthetized mice to measure the leg and toe responses following electrical stimulation *in vivo* (Fig. 5a; Supplementary Fig. 30). MECH electrodes conformably wrapped themselves around the sciatic nerve (Fig. 5b) to enable intimate contacts (Fig. 5c) and reduced tissue–electrode impedance. In addition, their good elasticity together with low Young's modulus values enabled the implanted MECH electrode to stretch and maintain close contact with the sciatic nerves during the recurrent leg movement. Moreover, encapsulated MECH microelectrodes provided localized stimulation on subgroups of peripheral nerve bundles to control individual toe movements in accordance to the stimulation frequency

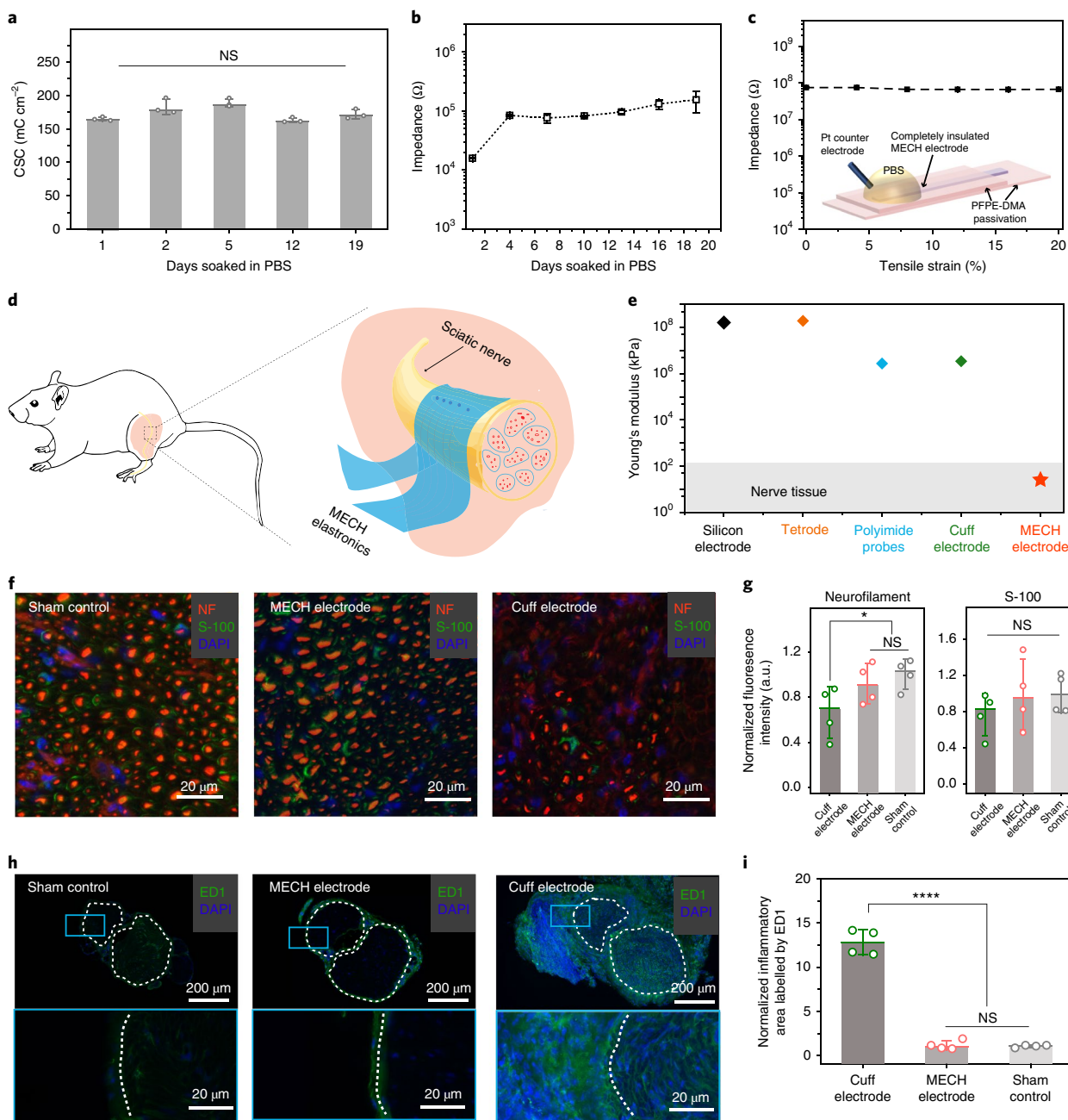


**Fig. 3 | Aqueous stability and biocompatibility.** **a**, Characterization of the CSC of an ECH ( $n=3$ ) incubated in PBS over 19 days,  $P>0.05$  (to 1-day as comparison,  $P=0.151$  (2-day),  $P=0.0513$  (5-day),  $P=0.998$  (12-day) and  $P=0.814$  (19-day), via one-way analysis of variance). **b**, Impedance stability at 1 kHz of MECH microelectrode ( $20\ \mu\text{m} \times 1\ \text{mm}$  with thickness of  $200\ \text{nm}$ ,  $n=3$ ) soaked in PBS solution for 19 days. **c**, The impedance of MECH electrodes insulated by PFPE-DMA at 1 kHz were higher than  $100\ \text{M}\Omega$  and were unaffected after applied strain. Inset: schematics of the measurement set-up for capacity of insulation, in which electrodes ( $n=3$ ) were completely insulated by PFPE-DMA. **d**, Schematic of the biocompatibility study. A MECH electrode array encapsulated with PFPE-DMA elastomer with  $200\ \mu\text{m} \times 200\ \mu\text{m}$  exposed MECH regions was wrapped around the sciatic nerve of the mice for 6 weeks. **e**, Comparison of the Young's modulus values of the MECH electrode with that of nerve tissue (grey rectangle) and with those of the following conventional implantable electrical probes: silicon electrode<sup>56</sup>, tetrode<sup>57</sup> and planar polyimide probes<sup>58</sup> and flexible Au-PET cuff electrode. **f**, Z-projection of a confocal micrograph of immunochemically labelled cross-section slice of sciatic nerve. The pseudocolour coding shows the biomarker S-100 in green and neurofilament (NF) in red for the sham control, the MECH electrode and the high modulus plastic cuff electrode. DAPI, 4',6'-diamidino-2-phenylindole. **g**, Histogram showing the mean fluorescence intensity of neurofilaments and Schwann cells (labelled by S-100) in the sham control, the MECH electrode and the cuff electrode. The  $P$  values for comparison of the neurofilament intensities are as follows: for the cuff electrode versus the MECH electrode,  $P=0.043$ ; for the cuff electrode versus the sham control,  $P=0.027$ ; and for the MECH versus sham control,  $P=0.97$ . The  $P$  values for comparison of the S-100 intensities are as follows: for the cuff electrode versus the MECH electrode,  $P=0.366$ ; for the cuff electrode versus the sham control,  $P=0.957$ ; and for the MECH versus the sham control,  $P=0.193$ . \* $P<0.05$ . **h**, Cross-section slice of a sciatic nerve labelled by the inflammatory biomarker ED1 for the sham control, the MECH electrode and the cuff electrode. Inset: a zoomed-in image at the nerve bundle interface. **i**, Histogram showing the normalized inflammatory area labelled by anti-ED1 antibody. The  $P$  values for comparison of the neurofilament intensities are as follows: for the cuff electrode versus the MECH electrode,  $P=4.721 \times 10^{-6}$ ; for the cuff electrode versus the sham control,  $P=3.204 \times 10^{-6}$ ; and for the MECH versus the sham control,  $P=0.6973$ . \*\*\*\* $P<0.0001$ . Unpaired, two-tailed  $t$ -test ( $n=4$ ) was used for statistical analyses in **i** and **g**. All error bars denote the s.d. NS, not significant.

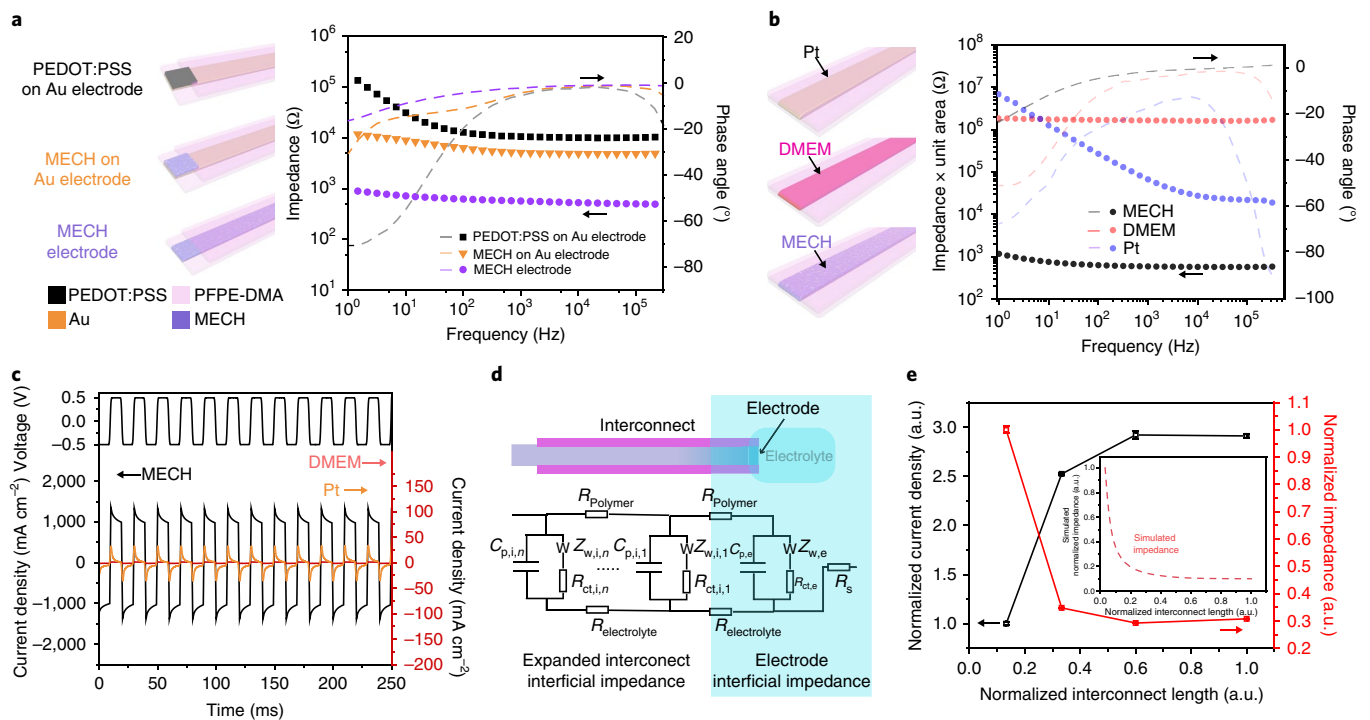


**Fig. 4 | MECHs display high current density and low impedance.** **a**, The impedance spectra of PEDOT:PSS on an Au electrode, a MECH on an Au electrode and a MECH electrode. All electrodes had the same exposed electrode area of  $0.5 \text{ mm}^2$ . The MECH electrode was patterned for both solution contact and interconnect, while the MECH on an Au electrode was fabricated by coating the tip of an Au electrode with a MECH for solution contact only. For the PEDOT:PSS on an Au electrode, silane-crosslinked PEDOT:PSS was used as the solution contact and Au was used as interconnect. The scatter plot represents the impedance magnitude, while the broken line represents the phase angle. **b**, Impedance spectra of a pure electronic conductor (platinum), a pure ionic conductor (DMEM) and the dual-conductor MECH. Only the cross-sectional area of the interconnect was exposed to solution. The scatter plot represents the impedance magnitude, while the broken lines represent the phase angle. **c**, Current densities of platinum and DMEM measured at a frequency of 50 Hz, with  $\pm 0.5$  V bipolar pulses. **d**, Transmission line model of a conductive hydrogel as both the electrode and interconnect. Interconnect Randel circuits that consists of interconnect volumetric double-layer capacitance,  $C_{p,i,n}$  interconnect reaction resistance,  $R_{ct,i,n}$  and interconnect Warburg element,  $Z_{w,i,n}$  are in parallel with electrode Randel circuit that consists of electrode double-layer capacitance,  $C_{p,e}$  electrode reaction resistance,  $R_{ct,e}$  and electrode Warburg element  $Z_{w,e}$ . Diffusion of the electrolyte into the hydrogel interconnect increases the number of interconnect Randel circuits,  $n$ , which is in parallel with the electrode Randel circuit, leading to the decrease in the overall impedance. **e**, Geometry-dependent current density and impedance for the MECH ( $n=3$ ). The current density increases correspondingly when the interconnect length increases. Inset: simulated impedance versus interconnect length based on the transmission line model in the main image. Error bars denote the s.d.

(Fig. 5d; Supplementary Video 2). Our MECH electrode stimulated leg response at an ultralow voltage of 50 mV, without the need to remove or penetrate the epineurium layer (Fig. 5e). The result was further validated through the successful recording of intramuscular electromyogram (EMG) traces at a voltage of 50 mV (Supplementary Fig. 31). By contrast, conventional platinum electrodes (with the same dimension) required at least 500 mV to achieve observable leg movements (Supplementary Video 3). Furthermore, the range of leg movement induced by the MECH electrode was significantly higher than that of the platinum electrode (again with the same electrode area) from 50 mV to 1 V. Notably, 6 weeks after implantation in mice, the impedance of the MECH electrodes decreased while the capacitance per unit area increased (Supplementary Fig. 32). Our MECH electrode can elicit an even larger leg response after 2 months of soaking in PBS, thus validating the long-term electrochemical stability of our MECH electrode and suggesting that continuous swelling of the porous MECH network in aqueous solution resulted in a further lowering of the impedance values (Fig. 5f).

The materials, device structure and microfabrication techniques developed for MECH elastronics could serve as a useful technology for fabricating other soft medical electronics. Specifically, the entire device, including the interconnect, mimics the mechanical

properties of biological tissues. This significantly reduced the mechanical discrepancy at the bioelectronic interface, which could improve mechanical coupling and reduce the immune response from biological systems during long-term implantation. Looking forward, we anticipate that MECH elastronics can be used for implantable neuromodulation devices, such as deep brain stimulators and vagus nerve stimulators. For clinical applications, the ease of use and robustness of implantable electronics are important. Instead of relying entirely on reducing the thickness of the device to achieve a lower bending stiffness, here, we offer an alternative strategy through reducing the Young's modulus of electronic materials. Thus, the thickness of the device is maintained, offering ease of handling and the potential to further incorporate multilayered, multifunctional structures. In addition, low-voltage electrical stimulation at 50 mV on a peripheral nerve was demonstrated in live mice, suggesting a strategy to further lower the voltage constraint on designing power systems in current implantable electronics. The elastronics demonstrated in this study represent an important step towards tissue-like electronics. We envision that additional features, such as system integration of large-scale microelectrodes, electrophysiological recording and biomolecular sensing, can be potentially integrated into our MECH elastronics for producing the next generation of multifunctional and miniaturized soft electronics.

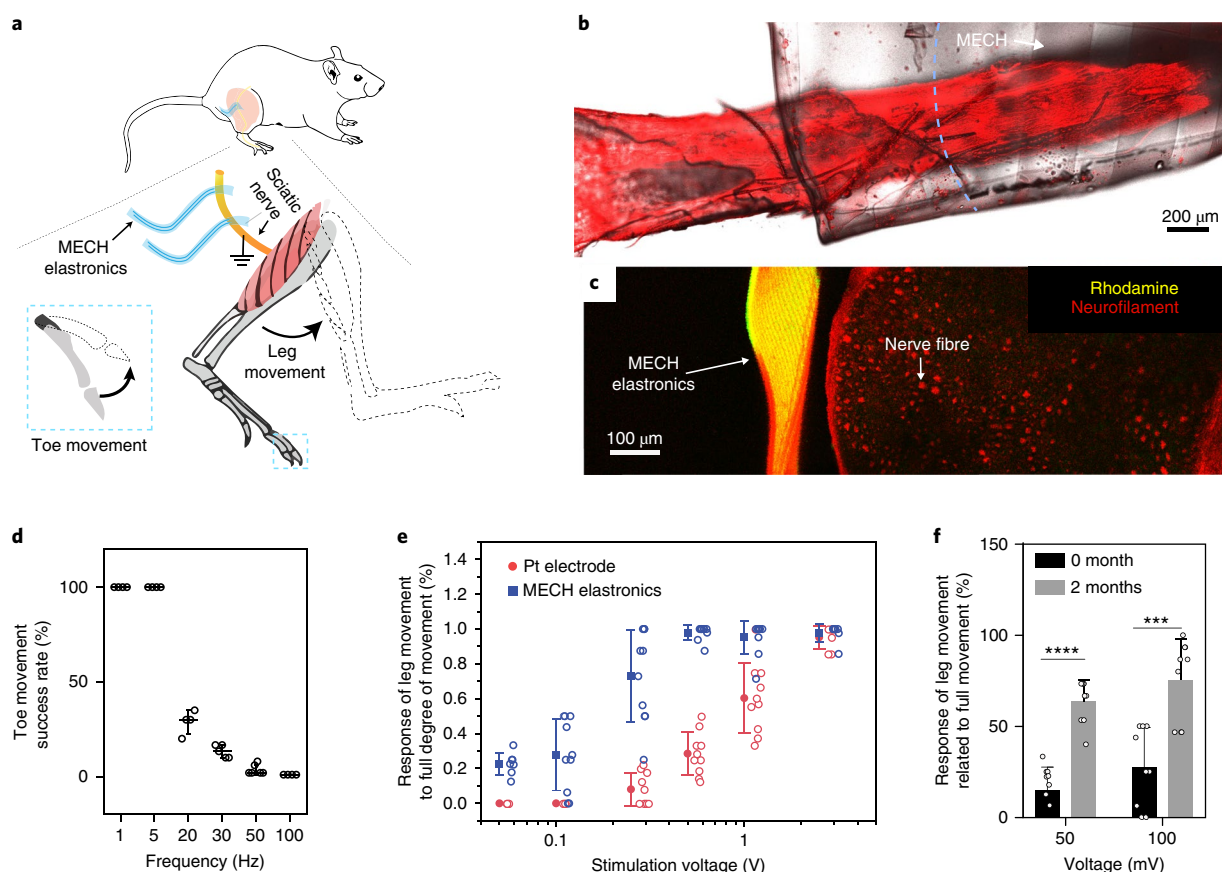


**Fig. 5 | Low-voltage in vivo neural stimulation.** **a**, Schematic of the in vivo neural stimulation experiment with a MECH microelectrode. Leg swing was stimulated by an electrode with a size of  $0.2\text{ mm} \times 3\text{ mm}$ , and the individual toe movement was achieved by localized stimulation with a microelectrode. **b**, Projection of a three-dimensional reconstructed confocal micrograph of the MECH microelectrodes on a soft elastic substrate conformably wrapping around a sciatic nerve. Neurofilament (red) was used to label neurons. The curved transparent sheet is the PFPE-DMA, while the dark lines are the MECH electrodes. **c**, Cross-sectional image along the dashed line in **b**. Outer surface of the sciatic nerve (red) is in close contact with the MECH electrodes (orange). **d**, Response of the toe movement under different stimulation frequencies with a charge balanced voltage pulse (pulse width of  $200\ \mu\text{s}$ , pulse amplitude of  $500\text{ mV}$ ;  $n=4$ ). **e**, The percentage of leg movement with respect to the full degree of movement under different stimulation voltages for the MECH electrode and the platinum electrode with the same exposed area ( $n=9$ ). **f**, After 2 months of soaking in PBS, the MECH electrodes stimulated an even higher percentage of leg movement with respect to the full degree of movement at  $50\text{ mV}$  and  $100\text{ mV}$ . For  $50\text{ mV}$  stimulation,  $P=4.92 \times 10^{-7}$ , for  $100\text{ mV}$  stimulation,  $P=0.000295$ .  $***P < 0.001$ ,  $****P < 0.0001$  ( $n=9$ , unpaired, two-tailed *t*-test). Error bars denote the s.d.

## Methods

**Material preparation.** *Preparation of PEDOT:PSS ECH.* PEDOT:PSS (PH1000) and the ionic liquid (4-(3-butyl-1-imidazolium)-1-butanesulfonic acid triflate) were purchased from Clevios and Santa Cruz Biotechnology, respectively. Approximately 50 wt% of ionic liquid versus PEDOT:PSS was added to PEDOT:PSS aqueous solution ( $0.172\text{ g}$  in  $15\text{ ml}$  of PH1000 solution) and stirred vigorously for 20 min. The PEDOT:PSS–ionic liquid aqueous mixture was then filtered through a  $0.45\text{-}\mu\text{m}$  syringe filter. For thin-film preparation, the filtered PEDOT:PSS–ionic liquid solution was spin coated on  $\text{SiO}_2$ , PFPE or PDMS substrate at a speed of  $2,000\text{ r.p.m.}$  for 1 min, followed by annealing at  $130^\circ\text{C}$  for 30 min. The substrates were treated with oxygen plasma (Technics Micro-RIE Series 800) at  $150\text{ W}$  for 1 min before spin coating. The bulk film was obtained by drying the mixture overnight in a Teflon mould and baking at  $130^\circ\text{C}$  for 30 min. In the ionic liquid–water exchange step, the film was soaked in a copious amount of deionized water (Millipore water purification system) for over 24 h. Deionized water was replaced every 8 h. The obtained MECH film was dehydrated at  $130^\circ\text{C}$  for 30 min and rehydrated by soaking in water for multiple cycles. The control sample, pristine PEDOT:PSS, was prepared using the same method described above except without the addition of ionic liquid. Another control sample, silane (3-glycidioxypropyltrimethoxysilane (GOPS)) cross-linked PEDOT:PSS, was prepared by mixing 1% GOPS in PH1000 solution and drop cast or spin coated at  $2,000\text{ r.p.m.}$

*Synthesis of PFPE-DMA.* Scheme 1 in the Supplementary Information shows the synthesis process of PFPE-DMA. This process is the same as that previously reported<sup>67</sup>. Briefly, the PFPE diols ( $4\text{ kg mol}^{-1}$ ) were obtained from Daikin

Co. or Solvay Specialty Polymer. The PFPE diols were first dissolved in 1,1,1,3,3-pentafluorobutane and reacted at room temperature with isophorone diisocyanate at a 3:2 molar ratio for 48 h to yield the chain-extended PFPE diols. Then, the product was reacted with 2-isocyanatoethyl methacrylate (IEM) at a 3:2 molar ratio ( $4\text{ kg mol}^{-1}$  PFPE diols:IEM) at room temperature for 24 h. In both reactions,  $0.1\text{ wt}\%$  tetrabutyltin diacetate was used as the catalyst. The final product was filtered through a  $0.2\text{-}\mu\text{m}$  syringe filter to yield a clear and colourless oil. The solvent was removed by rotary evaporation.

**Device fabrication.** A dextran (09184, Sigma-Aldrich) aqueous solution ( $5\text{ wt}\%$ ) was spin coated on a Si wafer as the sacrificial layer. A PDMS substrate was made by spin coating from Sylgard 184 (PDMS:crosslinker 10:1 weight ratio) at a speed of  $1,000\text{ r.p.m.}$  for 1 min, and followed by annealing at  $130^\circ\text{C}$  for 30 min. The substrate was treated with oxygen plasma (Technics Micro-RIE Series 800) at  $150\text{ W}$  for 1 min before spin coating. PFPE-DMA dissolved in 1,3-bis(trifluoromethyl)benzene (99%, catalogue number 251186, Sigma-Aldrich) solution was spin coated on the PDMS at  $1,500\text{ r.p.m.}$  for 1 min in a  $\text{N}_2$  glovebox (mBRAUN Glove Box System). The PFPE-DMA layer was cured via UV light (UV Nail Lamp,  $340\text{--}380\text{ nm}$  wavelength,  $36\text{ W}$ ) for 5 min, followed by baking at  $180^\circ\text{C}$  for 1 h and subsequently treated by oxygen plasma at  $150\text{ W}$  for 1 min. The PEDOT:PSS–ionic liquid aqueous mixture was drop cast or spin coated ( $2,000\text{ r.p.m.}$ , 1 min) on the oxygen plasma-treated PFPE-DMA layer and baked at  $130^\circ\text{C}$  for 30 min. A layer ( $40\text{ nm}$ ) of Au was subsequently deposited by e-beam evaporation (KJ Lesker evaporator). S1805 photoresist was spin coated on the Au at  $4,000\text{ r.p.m.}$  for 45 s and exposed with mask aligner (Quintel Q4000) for 3 s at a power of  $10\text{ mW cm}^{-2}$  after  $115^\circ\text{C}$  pre-expose baking (1 min). The

exposed photoresist was developed in MF-319 developer (Micropost) for 1 min. Micropatterns of S1805 were transferred to the Au by etching using argon ion milling (Intlvac Nanoquest Ion Mill, bias voltage 100 V) for 1 min. Inductively coupled plasma etching (600 W, 80 sccm; PlasmaTherm Oxide Etcher) or oxygen plasma (300 W, 8 sccm; March PX-250 Plasma Asher) was used to etch PEDOT:PSS-ionic liquid ion gel and remove the photoresist. Then, the Au layer on PEDOT was removed by argon ion milling etching for 1 min. The sample was submerged in water to remove ionic liquid and dried by baking at 130 °C for 30 min. The encapsulating PFPE-DMA with 2 wt% photoinitiator bis(2,4,6-trimethylbenzoyl)-phenylphosphineoxide (catalogue number 511447, Sigma-Aldrich) in bis(trifluoromethyl)benzene (1 g ml<sup>-1</sup>) was spin coated at 500 r.p.m. for 1 min and then prebaked at 100 °C for 1 min. UV exposure (Quintel Q4000, Hg Lamp, 350–450 nm) at 10 mW cm<sup>-2</sup> for 20 s was used to crosslink PFPE-DMA. For imaging samples used in the biocompatibility test, rhodamine-6G (1 µg ml<sup>-1</sup>; catalogue number 252433, Sigma-Aldrich) was added in the PFPE-DMA solution as the top insulation layer. The UV-exposed PFPE-DMA was developed in 1,3-bis(trifluoromethyl)benzene for 1 min. Finally, the freestanding MECH device was obtained by soaking in water for at least 1 day and subsequently the entire film was released from the dextran sacrificial layer.

**Characterization. Conductivity characterization.** A freestanding ECH with dimensions of 2 × 14 mm with an initial thickness of 30 µm was measured. The resistance (*R*) of the hydrogel was measured using the direct current (d.c.) four-point probe method with a Keithley 2400 Source Meter at room temperature. The width (*w*) and length (*l*) of the film during the ion gel to hydrogel transition was measured by a caliper. The thickness (*t*) was measured with a micrometer or an optical microscope. The conductivity ( $\sigma$ ) was calculated using the following equation:

$$\sigma = \frac{1}{R} \cdot \frac{l}{w \cdot t}$$

The data collected using the above method are shown in Fig. 1c.

**Morphological and chemical characterization.** SEM imaging was carried out on a FEI XL30 Sirion scanning electron microscope. The drop-casted MECH samples were freeze-dried before SEM imaging. Liquid nitrogen was used to freeze the sample. The elemental composition of the dehydrated MECH was measured using a Scanning XPS Microprobe (Physical Electronics VersaProbe III) with a monochromatic Al K-alpha X-ray source. Sputtering was performed at 10 kV and 20 mA with a C60 ion sputtering gun to preserve the chemical information in the polymer films. The atomic ratio was calculated by averaging the elemental composition on four sputtered depths at binding energies corresponding to nitrogen, fluorine and sulfur in high-resolution mode.

**Mechanical characterization.** Nanoindentation experiments were performed on fully hydrated MECHs submerged in deionized water using a Park NX10 AFM. The deflection sensitivity of the AFM cantilever was calibrated on a stiff substrate (Si) before the nanoindentation experiment on the conductive hydrogel. An AFM cantilever (CP-PNPL-SiO-A, sQUBE) with a spring constant of 0.08 N m<sup>-1</sup> and a microsphere of 2 µm in diameter on its tip was used to indent the sample. The Young's modulus of the hydrogel was calculated using SPII software.

The viscoelastic property of the conductive hydrogel and the hydrated pristine PEDOT:PSS was measured using a rheometer (TA Instrument ARES-G2). The MECH sheet was cut into an 8-mm diameter disc to match the plate diameter. The rheological measurement was performed with a frequency sweep measurement from 10 Hz to 0.01 Hz with 2% strain.

**Electrical and electrochemical characterization under uniaxial stretching.** The electrochemical impedance and CV were measured with a potentiostat (Biologic VSP-300 work station) in DMEM (1×, ThermoFisher Scientific). A platinum electrode was used as the counter electrode. Potentiostatic electrochemical impedance spectroscopy (PEIS) was performed with a sine wave (frequency from 1 Hz to 1 MHz) and a signal amplitude of 10 mV. The CV was recorded at a scan rate of 20 mV s<sup>-1</sup> versus an Ag/AgCl (3 M KCl) reference electrode from -0.6 V to 0.8 V.

For the ECH stretchability test, a thin-film ECH (200 nm in thickness) was prepared on a PDMS (Sylgard 184, 1:20 PDMS: crosslinker weight ratio) substrate. The ECH film was used as both the electrode and interconnect. The ECH film was first dehydrated by baking at 130 °C for 30 min and then patterned by oxygen plasma dry etching (150 W, 3 min) through a shadow mask. A 5 mm × 5 mm area ECH was obtained and exposed for solution contact, while rest areas were insulated by PDMS (1:20). The film was subsequently hydrated by soaking in DMEM for 2 h. Liquid metal EGaIn was used to make contact. The ECH electrode on PDMS was directly anchored on a home-built stretch station. The PEIS was performed using 0 to 20% strain. The stretch cycling test was conducted for 10,000 cycles using the home-built stretch station while the resistance was measured with a LCR meter (Keysight Technologies E4980). The dielectric constant of PFPE-DMA was measured at 1 kHz with a LRC meter by sandwiching PFPE-DMA in between two 6 mm × 6 mm aluminium electrodes.

**Stability characterization in aqueous solution.** UV-visible adsorption (Agilent Cary 6000i UV/Vis/NIR) was used for testing the stability of thin-film ECH and PEDOT:PSS film coated on glass slides. The UV-visible adsorption spectra were acquired at 0 h, 6 h and 24 h after soaking the samples in water. The weight loss in the deionized water for both ECH and PEDOT:PSS films was calculated by measuring the retained dry mass with a microbalance each week for 3 weeks. To test the stability of the electrochemical properties, PEIS and CV were performed at days 1, 2, 5, 12 and 19 of soaked samples. A small PDMS chamber was used to contain PBS (0.1 M, pH 7.4) to prevent water evaporation during the sample soaking in PBS. Au-deposited flexible PET was directly pressed against a MECH interconnect to make contact between the MECH and the measurement equipment.

**Impedance and current density characterization.** To evaluate the contribution of the MECH interconnect, the MECH electrode with both MECH solution contact and MECH interconnect was compared against PEDOT:PSS on an Au electrode and the MECH on an Au electrode. The exposed area of the MECH and PEDOT:PSS were kept the same at 1 mm × 0.5 mm, while the encapsulated MECH was 30 mm in length and 0.5 mm in width at 30 µm dry thickness. The Au interconnect was 0.5 mm in width, 30 mm in length and 40 nm in thickness. To further demonstrate the importance of porous interconnects filled with electrolyte, the impedance and current density of the MECH electrode was compared with DMEM and platinum electrodes. The impedance and current density were normalized to the same exposed electrode area of 0.06 mm<sup>2</sup>. The MECH and platinum electrode were prepared by cutting the encapsulated MECH or platinum interconnect and exposing the cross-section for solution contact. For measuring DMEM, a microfluidic channel was filled with DMEM. A pulse measure unit and a 4225-remote preamplifier/switch module (Keithley 4200-SCS) were used for current density characterization via ultrafast current-voltage measurements. We applied square wave voltages at 50 Hz, and currents were recorded simultaneously for calculation of the current densities. For the geometry-dependent current density measurement, the current was measured with a MECH interconnect at different lengths (from 2 mm to 5 mm). Au-deposited flexible PET was used as the contacts for the current density characterization. The impedance simulation was based on a simplified transmission line model.

**In vivo sciatic nerve interfacing. Mice preparation.** Adult (25–35 g) male C57BL/6J mice (Jackson Laboratories) were group-housed, given access to food pellets and water ad libitum and maintained on a 12 h:12 h light: dark cycle. All animals were held in a facility next to the laboratory 1 week before surgery, post-surgery and throughout the duration of the behavioural assays to minimize stress from transportation and disruption from foot traffic. All procedures were approved by the Animal Care and Use Committee of Stanford University (protocol APLAC-31893) and conform to US National Institutes of Health guidelines.

**In vivo electrical stimulation.** After animals were acclimated to the holding facility for more than 1 week, isoflurane was used to anaesthetize the mice. A heating pad at 37 °C was placed underneath the body. The depth of anaesthesia was monitored by pinching the feet of the mice periodically. A 2-cm incision of the skin was made, and the sciatic nerve was exposed by separating muscles close to the femur. Autoclaved sticks were inserted below the sciatic nerve. A MECH elastronic electrode or a platinum wire with an electrode area of 0.09 mm<sup>2</sup> was gently placed on the exposed sciatic nerve for electrical stimulation. For the leg movement experiment, 100 Hz, biphasic charge balanced rectangular voltage pulses (200 µs pulse width) were applied by using a function generator (PCSGU250, Velleman). The leg response was recorded using a digital microscope. Protractor markers printed on paper were placed under the leg to measure the swing angle. EMG was used to record muscle activity during electrical stimulation of the sciatic nerve. Three needle electrodes were used to penetrate the muscles, and the electrodes were connected to a signal acquisition system (Muscle SpikerBox, Backyard Brain). Various voltage amplitudes (from 50 mV to 500 mV) were used to stimulate the sciatic nerve while EMG traces was recorded. For the individual toe movement experiment, a 20-µm wide electrode (2-mm long) was used to make localized contact with the sciatic nerve, and an electrode with an electrode area of 0.09 mm<sup>2</sup> was used as the counter electrode. The toe movement success rate was calculated as the percentage of individual toe movement of the total number of stimulation pulses. The toe movement success rate was measured at various stimulation frequencies. The mice were killed immediately after the experiment.

**Chronic implantation.** The fabricated MECH elastronics and cuff electrodes were cleaned by UV Ozone (UVO-Cleaner Model 42) treatment for 20 min. The cuff electrode was fabricated via the thermal evaporation of Au (40 nm) on a PET substrate (100 µm). For imaging, samples were labelled with rhodamine-6G and the excess rhodamine-6G was washed away by soaking in PBS for 2 days. Before implantation, the electrodes were soaked in ethanol for 1 h and washed in a PBS solution for 5 min. Mice were anaesthetized by isoflurane, and the sciatic nerve was prepared as per the "In vivo electrical stimulation" section. The electrodes were wrapped around the sciatic nerve, guided by microscopy imaging. After implantation, the skin was sutured with surgical knots. Anti-inflammatory

and antibacterial ointment was swabbed onto the skin after surgery. A 0.3-ml intraperitoneal injection of Buprenex (Patterson Veterinary Supply; diluted with 0.5 ml of PBS) was administered at 0.1 mg per kg to reduce post-operative pain. Animals were observed for 4 h after surgery. To study the volumetric effect of the electrode on impedance and capacitance, pre-soaked MECH electrodes (in PBS for 1 day) were implanted around the sciatic nerve for 6 weeks. The impedance spectrum was measured before and after implantation. All procedures complied with the US Department of Agriculture guidelines for the care and use of laboratory animals and were approved by the Administrative Panel on Laboratory Animal Care (protocol APLAC-31893, Stanford University).

**Immunostaining.** Biocompatibility studies were performed to compare nerve bundle damage and immune responses at the implantation site for the MECH electrode, the cuff electrode and the sham control. Four mice were used for each case. Six weeks after implantation, the mice were killed. The legs with implants were fixed in a PBS solution with 4 wt% formaldehyde for 24 h. Fixed legs were first transferred to a sucrose solution (30%) overnight, then transferred to a sucrose-Cryo-OCT compound (VWR International) solution for 8 h and finally transferred to Cryo-OCT compound and frozen at  $-80^{\circ}\text{C}$ . The frozen samples were sectioned into 30- $\mu\text{m}$  tissue slices using a Leica CM1950 cryosectioning instrument (Leica Microsystems).

Neurofilament and S-100 protein in the tissue slices were stained for imaging. The slices were washed with PBS three times and then permeabilized by 0.1% Triton-X 100 in PBS for 15 min. After washing with PBS solution, the samples were incubated in blocking solution (3% bovine serum albumin, 0.1% Triton-X 100 in PBS) for 45 min. The samples were then co-stained with 1:100 anti-S100 (ab52642, Abcam) and 1:1,000 anti-neurofilament (ab8135, Abcam) in blocking solution overnight at  $4^{\circ}\text{C}$ . The samples were washed with PBS and stained with secondary antibody anti-rabbit IgG H&L (Alexa Fluor 488, ab150077) and anti-mouse IgG H&L (Alexa Fluor 647, ab150115). Anti-TNF $\alpha$  (sc-52746, dilution 1:50) and anti-ED1 (MAB1435, dilution 1:200) were used to characterize inflammatory responses. Epifluorescence and confocal images of the samples were taken using an Inverted Zeiss LSM 780 multiphoton laser scanning microscope. The fluorescence intensity and inflammatory tissue area were normalized to the mean value of the sham control. Unpaired, two-tailed *t*-tests were performed using Prism.

**Reporting Summary.** Further information on experimental design is available in the Nature Research Reporting Summary linked to this article.

## Data availability

The authors declare that all data supporting the findings of this study are available within the paper and its Supplementary Information.

Received: 3 April 2018; Accepted: 27 November 2018;

Published online: 8 January 2019

## References

- Kringelbach, M. L., Jenkinson, N., Owen, S. L. F. & Aziz, T. Z. Translational principles of deep brain stimulation. *Nat. Rev. Neurosci.* **8**, 623–635 (2007).
- Borovikova, L. V. et al. Vagus nerve stimulation attenuates the systemic inflammatory response to endotoxin. *Nature* **405**, 458–462 (2000).
- Lacour, S. P., Courtine, G. & Guck, J. Materials and technologies for soft implantable neuroprostheses. *Nat. Rev. Mater.* **1**, 16063 (2016).
- Feiner, R. & Dvir, T. Tissue-electronics interfaces: from implantable devices to engineered tissues. *Nat. Rev. Mater.* **3**, 17076 (2017).
- Salatino, J. W., Ludwig, K. A., Kozai, T. D. Y. & Purcell, E. K. Glial responses to implanted electrodes in the brain. *Nat. Biomed. Eng.* **1**, 862–877 (2017).
- Someya, T., Bao, Z. & Malliaras, G. G. The rise of plastic bioelectronics. *Nature* **540**, 379–385 (2016).
- Khodagholy, D. et al. NeuroGrid: recording action potentials from the surface of the brain. *Nat. Neurosci.* **18**, 310–315 (2015).
- Canales, A. et al. Multifunctional fibers for simultaneous optical, electrical and chemical interrogation of neural circuits in vivo. *Nat. Biotechnol.* **33**, 277–284 (2015).
- Kim, J. et al. Stretchable silicon nanoribbon electronics for skin prosthesis. *Nat. Commun.* **5**, 5747 (2014).
- Xu, L. et al. 3D multifunctional integumentary membranes for spatiotemporal cardiac measurements and stimulation across the entire epicardium. *Nat. Commun.* **5**, 3329 (2014).
- Liu, J. et al. Syringe-injectable electronics. *Nat. Nanotechnol.* **10**, 629–636 (2015).
- Mineev, I. R. et al. Electronic dura mater for long-term multimodal neural interfaces. *Science* **347**, 159–163 (2015).
- Hong, G., Yang, X., Zhou, T. & Lieber, C. M. Mesh electronics: a new paradigm for tissue-like brain probes. *Curr. Opin. Neurobiol.* **50**, 33–41 (2018).
- Jeong, J. W. et al. Soft materials in neuroengineering for hard problems in neuroscience. *Neuron* **86**, 175–186 (2015).
- Caliori, S. R. & Burdick, J. A. A practical guide to hydrogels for cell culture. *Nat. Methods* **13**, 405–414 (2016).
- Sharma, B. et al. Human cartilage repair with a photoreactive adhesive-hydrogel composite. *Sci. Transl. Med.* **5**, 167ra6 (2013).
- Yuk, H., Zhang, T., Lin, S., Parada, G. A. & Zhao, X. Tough bonding of hydrogels to diverse non-porous surfaces. *Nat. Mater.* **15**, 190–196 (2015).
- Kang, H.-W. et al. A 3D bioprinting system to produce human-scale tissue constructs with structural integrity. *Nat. Biotechnol.* **34**, 312–319 (2016).
- Keplinger, C. et al. Stretchable, transparent, ionic conductors. *Science* **341**, 984–987 (2013).
- Sekine, S., Ido, Y., Miyake, T., Nagamine, K. & Nishizawa, M. Conducting polymer electrodes printed on hydrogel. *J. Am. Chem. Soc.* **132**, 13174–13175 (2010).
- Sasaki, M. et al. Highly conductive stretchable and biocompatible electrode-hydrogel hybrids for advanced tissue engineering. *Adv. Healthc. Mater.* **3**, 1919–1927 (2014).
- Abidian, M. R. et al. Hybrid conducting polymer-hydrogel conduits for axonal growth and neural tissue engineering. *Adv. Healthc. Mater.* **1**, 762–767 (2012).
- Hassarati, R. T. et al. Improving cochlear implant properties through conductive hydrogel coatings. *IEEE Trans. Neural Syst. Rehabil. Eng.* **22**, 411–418 (2014).
- Abidian, M. R. & Martin, D. C. Multifunctional nanobiomaterials for neural interfaces. *Adv. Funct. Mater.* **19**, 573–585 (2009).
- Feig, V. R., Tran, H., Lee, M. & Bao, Z. Mechanically tunable conductive interpenetrating network hydrogels that mimic the elastic moduli of biological tissue. *Nat. Commun.* **9**, 2740 (2018); correction **9**, 5030 (2018).
- Green, R. A. et al. Conductive hydrogels: mechanically robust hybrids for use as biomaterials. *Macromol. Biosci.* **12**, 494–501 (2012).
- Amella, A. D. et al. Freestanding, soft bioelectronics. In *Proc. 7th International IEEE/EMBS Conference on Neural Engineering (NER)* 607–610 (IEEE, 2015).
- Ding, H. et al. Biologically derived soft conducting hydrogels using heparin-doped polymer networks. *ACS Nano* **8**, 4348–4357 (2014).
- Kim, D. H., Abidian, M. & Martin, D. C. Conducting polymers grown in hydrogel scaffolds coated on neural prosthetic devices. *J. Biomed. Mater. Res. A* **71**, 577–585 (2004).
- Kim, D. H., Wiler, J. A., Anderson, D. J., Kipke, D. R. & Martin, D. C. Conducting polymers on hydrogel-coated neural electrode provide sensitive neural recordings in auditory cortex. *Acta Biomater.* **6**, 57–62 (2010).
- Guisseppi-Elie, A. Electroconductive hydrogels: synthesis, characterization and biomedical applications. *Biomaterials* **31**, 2701–2716 (2010).
- Chung, D. *Materials for Electronic Packaging* (Butterworth-Heinemann, Newton, 1995).
- Yu, D., Yang, Y. Q., Chen, Z., Tao, Y. & Liu, Y. F. Recent progress on thin-film encapsulation technologies for organic electronic devices. *Opt. Commun.* **362**, 43–49 (2016).
- Wang, Y. et al. A highly stretchable, transparent, and conductive polymer. *Sci. Adv.* **3**, e1602076 (2017).
- Mawad, D., Lauto, A. & Wallace, G. G. In *Polymeric Hydrogels as Smart Biomaterials* (ed. Kalia, S.) 19–45 (Springer, New York, 2016).
- Strakosas, X. et al. A facile biofunctionalisation route for solution processable conducting polymer devices. *J. Mater. Chem. B* **2**, 2537–2545 (2014).
- Khodagholy, D. et al. High transconductance organic electrochemical transistors. *Nat. Commun.* **4**, 2133 (2013).
- Akhtar, R., Sherratt, M. J., Cruickshank, J. K. & Derby, B. Characterizing the elastic properties of tissues. *Mater. Today* **14**, 96–105 (2011).
- Patil, A. C. & Thakor, N. V. Implantable neurotechnologies: a review of micro- and nanoelectrodes for neural recording. *Med. Biol. Eng. Comput.* **54**, 23–44 (2016).
- Pan, L. et al. Hierarchical nanostructured conducting polymer hydrogel with high electrochemical activity. *Proc. Natl Acad. Sci. USA* **109**, 9287–9292 (2012).
- Green, R. A., Baek, S., Poole-Warren, L. A. & Martens, P. J. Conducting polymer-hydrogels for medical electrode applications. *Sci. Technol. Adv. Mater.* **11**, 014107 (2010).
- Yang, J., Choe, G., Yang, S., Jo, H. & Lee, J. Y. Polypyrrole-incorporated conductive hyaluronic acid hydrogels. *Biomater. Res.* **20**, 31 (2016).
- Chen, R., Canales, A. & Anikeeva, P. Neural recording and modulation technologies. *Nat. Rev. Mater.* **2**, 16093 (2017).
- Green, R. A. et al. Substrate dependent stability of conducting polymer coatings on medical electrodes. *Biomaterials* **33**, 5875–5886 (2012).
- Yamato, H., Ohwa, M. & Wernet, W. Stability of polypyrrole and poly(3,4-ethylenedioxythiophene) for biosensor application. *J. Electroanal. Chem.* **397**, 163–170 (1995).
- Thaning, E. M., Asplund, A. L. M., Nyberg, T. A., Inganäs, O. W. & von Holst, H. Stability of poly(3,4-ethylene dioxythiophene) materials intended for implants. *J. Biomed. Mater. Res. B Appl. Biomater.* **93**, 407–415 (2010).

47. Xiao, Y. et al. Synthesis and characterization of *p*-toluenesulfonate incorporated poly(3,4-ethylenedioxythiophene). *Talanta* **72**, 532–538 (2007).
48. Cogan, S. F. Neural stimulation and recording electrodes. *Annu. Rev. Biomed. Eng.* **10**, 275–309 (2008).
49. Wilks, S. Poly(3,4-ethylene dioxythiophene) (PEDOT) as a micro-neural interface material for electrostimulation. *Front. Neuroeng.* **2**, 7 (2009).
50. Rose, T. L. & Robblee, L. S. Electrical stimulation with Pt electrodes. VIII. Electrochemically safe charge injection limits with 0.2 MS pulses. *IEEE Trans. Biomed. Eng.* **37**, 1118–1120 (1990).
51. Goding, J., Gilmour, A., Martens, P., Poole-Warren, L. & Green, R. Interpenetrating conducting hydrogel materials for neural interfacing electrodes. *Adv. Healthc. Mater.* <https://doi.org/10.1002/adhm.201601177> (2017).
52. Mario Cheong, G. L. et al. Conductive hydrogels with tailored bioactivity for implantable electrode coatings. *Acta Biomater.* **10**, 1216–1226 (2014).
53. Grill, W. M. & Mortimer, J. T. Neural and connective tissue response to long-term implantation of multiple contact nerve cuff electrodes. *J. Biomed. Mater. Res.* **50**, 215–226 (2000).
54. Agnew, W. F., McCreery, D. B., Yuen, T. G. H. & Bullara, L. A. Histologic and physiologic evaluation of electrically stimulated peripheral nerve: considerations for the selection of parameters. *Ann. Biomed. Eng.* **17**, 39–60 (1989).
55. Larsen, J. O., Thomsen, M., Haugland, M. & Sinkjær, T. Degeneration and regeneration in rabbit peripheral nerve with long-term nerve cuff electrode implant: a stereological study of myelinated and unmyelinated axons. *Acta Neuropathol.* **96**, 365–378 (1998).
56. Schwarz, D. A. et al. Chronic, wireless recordings of large-scale brain activity in freely moving rhesus monkeys. *Nat. Methods* **11**, 670–676 (2014).
57. Lee, H., Bellamkonda, R. V., Sun, W. & Levenston, M. E. Biomechanical analysis of silicon microelectrode-induced strain in the brain. *J. Neural. Eng.* **2**, 81–89 (2005).
58. Rousche, P. J. et al. Flexible polyimide-based intracortical electrode arrays with bioactive capability. *IEEE Trans. Biomed. Eng.* **48**, 361–370 (2001).
59. Luan, L. et al. Ultraflexible nanoelectronic probes form reliable, glial scar-free neural integration. *Sci. Adv.* **3**, e1601966 (2017).
60. Zhou, T. et al. Syringe-injectable mesh electronics integrate seamlessly with minimal chronic immune response in the brain. *Proc. Natl Acad. Sci. USA* **114**, 5894–5899 (2017).
61. Rivnay, J. et al. Structural control of mixed ionic and electronic transport in conducting polymers. *Nat. Commun.* **7**, 11287 (2016).
62. Rivnay, J. et al. High-performance transistors for bioelectronics through tuning of channel thickness. *Sci. Adv.* **1**, e1400251 (2015).
63. Rivnay, J., Wang, H., Fenno, L., Deisseroth, K. & Malliaras, G. G. Next-generation probes, particles, and proteins for neural interfacing. *Sci. Adv.* **3**, e1601649 (2017).
64. Abidian, M. R. & Martin, D. C. Experimental and theoretical characterization of implantable neural microelectrodes modified with conducting polymer nanotubes. *Biomaterials* **29**, 1273–1283 (2008).
65. Williamson, A. et al. Localized neuron stimulation with organic electrochemical transistors on delaminating depth probes. *Adv. Mater.* **27**, 4405–4410 (2015).
66. Mawad, D. et al. A conducting polymer with enhanced electronic stability applied in cardiac models. *Sci. Adv.* **2**, e1601007 (2016).
67. Hu, Z. et al. Photochemically cross-linked perfluoropolyether-based elastomers: synthesis, physical characterization, and biofouling evaluation. *Macromolecules* **42**, 6999–7007 (2009).

## Acknowledgements

This work was partly supported by a Bio-X Interdisciplinary Initiatives Seed Grant and by BOE Technology Group Co., Ltd. Part of this work was performed at the Stanford Nano Shared Facilities (SNSF), supported by the National Science Foundation under award ECCS-1542152. Y.L. is supported by a National Science Scholarship (A\*STAR, Singapore). H.W. is supported by a NIH NRSA F32 postdoctoral fellowship. A.M.F. thanks the Natural Sciences and Engineering Research Council (NSERC) of Canada for a postdoctoral fellowship. X.W. is supported by a Life Science Research Foundation fellowship and the Gordon and Betty Moore Foundation. We thank X. Liu, Y. Li and K. Zhang from the BOE Technology Group Co., LTD for discussions, A. Tom for assistance with some experiments, and Daikin Co. and Solvay for supplying PFPE-diols.

## Author contributions

Y.L., J.L. and Z.B. designed the project and experiments. Y.L. synthesized the MECH. J.L. and T.L. synthesized the elastic fluorinated photoresist. Y.L. and J.L. fabricated the devices. Y.L., J.L., S.C. and Y.K. performed material and device characterization. Y.L., J.L. and A.M.F. prepared the schematics for electronics and carried out device photography. Y.L., J.L., X.W. and H.W. performed immunofluorescence staining and data analyses. S.N. and Y.L. carried out the simulation of electrochemical impedance. Y.L. and J.L. carried out periphery nerve stimulation experiments on mice and analysed the data. Y.L., J.L., J.B.-H.T. and Z.B. wrote the manuscript. All authors reviewed and commented on the manuscript.

## Competing interests

Stanford University has filed patent applications related to this technology. The patent application number is PCT/US2018/057855.

## Additional information

**Supplementary information** is available for this paper at <https://doi.org/10.1038/s41551-018-0335-6>.

**Reprints and permissions information** is available at [www.nature.com/reprints](http://www.nature.com/reprints).

**Correspondence and requests for materials** should be addressed to Z.B.

**Publisher's note:** Springer Nature remains neutral with regard to jurisdictional claims in published maps and institutional affiliations.

© The Author(s), under exclusive licence to Springer Nature Limited 2019

## Reporting Summary

Nature Research wishes to improve the reproducibility of the work that we publish. This form provides structure for consistency and transparency in reporting. For further information on Nature Research policies, see [Authors & Referees](#) and the [Editorial Policy Checklist](#).

### Statistical parameters

When statistical analyses are reported, confirm that the following items are present in the relevant location (e.g. figure legend, table legend, main text, or Methods section).

n/a | Confirmed

- The exact sample size ( $n$ ) for each experimental group/condition, given as a discrete number and unit of measurement
- An indication of whether measurements were taken from distinct samples or whether the same sample was measured repeatedly
- The statistical test(s) used AND whether they are one- or two-sided  
*Only common tests should be described solely by name; describe more complex techniques in the Methods section.*
- A description of all covariates tested
- A description of any assumptions or corrections, such as tests of normality and adjustment for multiple comparisons
- A full description of the statistics including central tendency (e.g. means) or other basic estimates (e.g. regression coefficient) AND variation (e.g. standard deviation) or associated estimates of uncertainty (e.g. confidence intervals)
- For null hypothesis testing, the test statistic (e.g.  $F$ ,  $t$ ,  $r$ ) with confidence intervals, effect sizes, degrees of freedom and  $P$  value noted  
*Give  $P$  values as exact values whenever suitable.*
- For Bayesian analysis, information on the choice of priors and Markov chain Monte Carlo settings
- For hierarchical and complex designs, identification of the appropriate level for tests and full reporting of outcomes
- Estimates of effect sizes (e.g. Cohen's  $d$ , Pearson's  $r$ ), indicating how they were calculated
- Clearly defined error bars  
*State explicitly what error bars represent (e.g. SD, SE, CI)*

*Our web collection on [statistics for biologists](#) may be useful.*

### Software and code

Policy information about [availability of computer code](#)

#### Data collection

Electrochemical-impedance and cyclic-voltammetry data were collected with EC-Lab, and mechanical tests were collected with Bluehill 3 Testing Software. Current-density data were collected by means of the Model 4200-SCS Keithley Test Environment Interactive (KTEI, Tektronix). UV-vis adsorption data were collected by using Cary WinUV software (Cary 6000i UV-Vis-NIR, agilent). Rheology data were collected by using TRIOS software (ARES-G2, TA instrument).

#### Data analysis

Electrochemical-impedance and cyclic-voltammetry data were analysed by using EC-Lab. Mechanical test data, UV-vis, rheology and current-density data were analysed by using OriginPro 2016 b9.3.226 (64-bit) and Microsoft Excel 2016 (version 1807, 10325.20082). Immunofluorescence data were analysed by using ImageJ (Fiji), OriginPro 2016 b9.3.226 (64-bit) and Microsoft Excel 2016 (version 1807, 10325.20082). Data from animal experiments were analysed by using custom code in Matlab R2017a.

For manuscripts utilizing custom algorithms or software that are central to the research but not yet described in published literature, software must be made available to editors/reviewers upon request. We strongly encourage code deposition in a community repository (e.g. GitHub). See the Nature Research [guidelines for submitting code & software](#) for further information.

## Data

Policy information about [availability of data](#)

All manuscripts must include a [data availability statement](#). This statement should provide the following information, where applicable:

- Accession codes, unique identifiers, or web links for publicly available datasets
- A list of figures that have associated raw data
- A description of any restrictions on data availability

The authors declare that all data supporting the findings of this study are available within the paper and its Supplementary Information.

## Field-specific reporting

Please select the best fit for your research. If you are not sure, read the appropriate sections before making your selection.

Life sciences  Behavioural & social sciences  Ecological, evolutionary & environmental sciences

For a reference copy of the document with all sections, see [nature.com/authors/policies/ReportingSummary-flat.pdf](https://www.nature.com/authors/policies/ReportingSummary-flat.pdf)

## Life sciences study design

All studies must disclose on these points even when the disclosure is negative.

Sample size

Data exclusions

Replication

Randomization

Blinding

## Reporting for specific materials, systems and methods

### Materials & experimental systems

n/a	Involvement
<input checked="" type="checkbox"/>	<input type="checkbox"/> Unique biological materials
<input type="checkbox"/>	<input checked="" type="checkbox"/> Antibodies
<input checked="" type="checkbox"/>	<input type="checkbox"/> Eukaryotic cell lines
<input checked="" type="checkbox"/>	<input type="checkbox"/> Palaeontology
<input type="checkbox"/>	<input checked="" type="checkbox"/> Animals and other organisms
<input checked="" type="checkbox"/>	<input type="checkbox"/> Human research participants

### Methods

n/a	Involvement
<input checked="" type="checkbox"/>	<input type="checkbox"/> ChIP-seq
<input checked="" type="checkbox"/>	<input type="checkbox"/> Flow cytometry
<input checked="" type="checkbox"/>	<input type="checkbox"/> MRI-based neuroimaging

## Antibodies

Antibodies used

Primary antibodies used in this work include anti-S100 (Abcam ab52642); anti-neurofilament (Abcam ab8135); Anti-TNF $\alpha$  (Santa Cruz Biotechnology, sc-52746); anti-ED1 (Millipore SigmaMAB1435); Secondary antibodies used in this work include Goat Anti-Rabbit IgG H&L (Alexa Fluor<sup>®</sup> 488) (Abcam ab150077), Goat Anti-Mouse IgG H&L (Alexa Fluor<sup>®</sup> 647) (Abcam ab150115).

Validation

Validation of each antibody was done under standard information offered by the supplier.

## Animals and other organisms

Policy information about [studies involving animals](#); [ARRIVE guidelines](#) recommended for reporting animal research

Laboratory animals

Adult (25–35 g, 4–8 weeks) male C57BL/6J mice were purchased from the Jackson Laboratory.

Wild animals

The study did not involve wild animals.

Field-collected samples

The study did not involve samples collected from the field.